Tidal Conversion by Supercritical Topography

NEIL J. BALMFORTH

University of British Columbia, Vancouver, British Columbia, Canada

THOMAS PEACOCK

Massachusetts Institute of Technology, Cambridge, Massachusetts

(Manuscript received 22 May 2008, in final form 20 January 2009)

ABSTRACT

Calculations are presented of the rate of energy conversion of the barotropic tide into internal gravity waves above topography on the ocean floor. The ocean is treated as infinitely deep, and the topography consists of periodic obstructions; a Green function method is used to construct the scattered wavefield. The calculations extend the previous results of Balmforth et al. for subcritical topography (wherein waves propagate along rays whose slopes exceed that of the topography everywhere), by allowing the obstacles to be arbitrarily steep or supercritical (so waves propagate at shallower angles than the topographic slopes and are scattered both up and down). A complicated pattern is found for the dependence of energy conversion on ϵ, the ratio of maximum topographic slope to wave slope, and the ratio of obstacle amplitude and separation. This results from a sequence of constructive and destructive interferences between scattered waves that has implications for computing tidal conversion rates for the global ocean.

1. Introduction

The generation of internal waves as the barotropic tide flows over topography on the ocean floor has lately received wide interest in view of observations by satellite altimetry (e.g., Egbert and Ray 2000) and the suggestions that the breaking of such waves could play an important role in setting up large-scale ocean circulation (Munk and Wunsch 1998); Garrett and Kunze (2007) offers a general review. A key issue is how much energy is converted into internal waves, a problem that has spawned a number of recent theoretical studies. Here we add some more results to this literature.

A previous article (Balmforth et al. 2002) explored a two-dimensional model of the generation process, building on earlier work by Bell (1975a,b). The topography was taken to be periodic, of gentle inclination, and lie underneath an ocean of infinite depth—assumptions that simplified the mathematics of the problem. The steepness of the topography can be quantified in terms of an important dimensionless parameter ϵ, which is the ratio of the maximum slope of the topography to the slope of the rays along which the radiated gravity waves propagate. As they are forced at the tidal frequency ω, these waves propagate along slopes that are fixed purely by the local buoyancy frequency N and Coriolis frequency f, which are independent of the shape of the scattering obstacle. Explicitly,

$$\epsilon = \sqrt{\frac{N^2-\omega^2}{\omega^2-f^2}}\,\max(|h_x|), \tag{1}$$

where $z = h(x)$ denotes the two-dimensional topographic surface, and $h_x \equiv dh/dx$.

In terms of ϵ, Bell's theory applies when $\epsilon \ll 1$. The work of Balmforth et al. (2002) applies when $\epsilon < 1$, or when the topography is "subcritical." However, neither approach can be used when $\epsilon > 1$, or when the topography is "supercritical." Our goal in this article is to extend the results to the supercritical regime.[1] To accomplish the task, we exploit the Green's function

Corresponding author address: Thomas Peacock, Mechanical Engineering, MIT, Cambridge, MA 02139.
E-mail: tomp@mit.edu

[1] Our current definition of ϵ is slightly different to that given by Balmforth et al. (2002). They defined this parameter in terms of a topographic height rather than the slope. We prefer (1) because it gives the criticality condition as $\epsilon = 1$.

DOI: 10.1175/2009JPO4057.1

techniques outlined by Petrelis et al. (2006) and Nycander (2006), who considered isolated, ridgelike topography in an ocean of finite depth and periodic knife edges in an infinitely deep ocean, respectively.

The results offer estimates of the rate at which barotropic tidal energy is converted into the internal tide, which can be compared with analogous results for isolated geometries (Llewellyn Smith and Young 2003; St. Laurent et al. 2003; Petrelis et al. 2006), and the numerical simulations of sinusoidal topography (Khatiwala 2003) and isolated steep topography (DiLorenzo et al. 2006). Importantly, by considering a periodic array of bumps, our study considers spatially extended topography that is more realistic than Nycander's (2006) knife edges and explores how conversion from a richer bottom structure is not merely akin to superposing isolated bumps. Altogether, our results serve to complete and unify several preceding articles.

2. Mathematical formulation

a. The wave equation

Our two-dimensional, horizontally periodic ocean model has infinite depth and constant buoyancy frequency N and Coriolis frequency f. The mathematical problem surrounds solving the internal wave equation

$$(\psi_{xx} + \psi_{zz})_{tt} + N^2\psi_{xx} + f^2\psi_{zz} = 0, \tag{2}$$

subject to the condition

$$\psi(x,\ h,\ t) = Uh(x)\cos\omega t, \tag{3}$$

applying on the topography [located at $z = h(x)$][2], an outgoing radiation condition for $z \to \infty$, and periodicity in x. Here, U is the tidal speed, ω is a tidal frequency, and the dependent variable $\psi(x, z, t)$ is the streamfunction from which we may rebuild the velocity field and buoyancy perturbations via

$$u = -\psi_z, \quad w = \psi_x, \quad \text{and} \quad b_t = -N^2\psi_x. \tag{4}$$

This formulation is inviscid, following the earlier studies of tidal conversion. Details of the derivation of these equations can be found in, for example, Balmforth et al. (2002).

We cast the problem into a convenient dimensionless form by setting

$$X = kx, \quad Z = kz\sqrt{\frac{N^2-\omega^2}{\omega^2-f^2}}, \quad \text{and}$$
$$\psi = Uh_m \mathrm{Re}[e^{-i\omega t}\varphi(X,Z)], \tag{5}$$

which incorporates the periodic time dependence at the tidal frequency expected in the steady-state scattering problem. The topography has a horizontal wavelength given by $2\pi/k$, and the characteristic height h_m is defined such that the dimensionless topography

$$H(X) \equiv \frac{h(x)}{h_m} \tag{6}$$

has a maximum slope of unity. Therefore,

$$\varphi_{XX} = \varphi_{ZZ}, \tag{7}$$

subject to the periodicity conditions $\varphi(0, Z) = \varphi(2\pi, Z)$ and $\varphi_X(0, Z) = \varphi_X(2\pi, Z)$, the inviscid boundary condition on the topography

$$\varphi[X, \epsilon H(X)] = H(X), \tag{8}$$

and the outgoing radiation condition applying for $Z \to \infty$.

Though by no means essential, the topography $H(X)$ is assumed to satisfy the reflection symmetry $H(X) = H(-X)$. The explicit example that we use is the "periodic Gaussian":

$$H(X) = \frac{e^{\gamma(\cos X - C_\gamma)}}{\sqrt{\gamma C_\gamma}} \quad \text{and} \quad C_\gamma = \frac{1}{2\gamma}\left(\sqrt{1+4\gamma^2}-1\right), \tag{9}$$

as introduced by Balmforth et al. (2002), although the current definition ensures that $\max(|H_X|) = 1$. Note that the dimensional peak-to-peak amplitude of the topography b is given by

$$b = h_m[H(0) - H(\pi)]. \tag{10}$$

The parameter γ controls the degree of isolation of the periodic bumps; in the limit $\gamma \to 0$, the topography converges to a sinusoid, whereas $H(X)$ increasingly resembles an array of widely separated and nearly Gaussian bumps as γ is increased.

b. The Green function solution

By suitably arranging an array of sources along the topography, the solution of (7) and (8) can be concisely expressed in terms of a Green function,

$$\varphi(X,Z) = \int_0^\pi \mathcal{G}[X, X', Z, \epsilon H(X')]\,\Gamma(X')\,dX', \tag{11}$$

[2] Note that this nonlinear boundary condition prevents one from linearly superposing solutions, which is a key simplification for the calculation of conversion rates of the global ocean using Bell's approximation (Nycander 2005).

where $\mathcal{G}(X, X', Z, Z')$ is the Green function and $\Gamma(X)$ is the source density. We use the Fourier series formula

$$\mathcal{G} = \sum_{p=1}^{\infty} \frac{\cos pX \cos pX'}{\pi p} \left(e^{-ip|Z-Z'|} - e^{-ip|Z+Z'|}\right) + \frac{i}{2\pi}(|Z+Z'| - |Z-Z'|); \quad (12)$$

much more information about this function is given in the appendix. Suffice to say that the formula automatically incorporates the periodicity requirement in X and applies the outgoing radiation condition for $Z \to \infty$.

The source density is fixed once we impose the inviscid boundary condition (8), which furnishes the integral equation

$$H(X) = \int_0^{\pi} \mathcal{G}[X, X', \epsilon H(X), \epsilon H(X')]\Gamma(X')dX'. \quad (13)$$

With the Fourier series (12) and a clever numerical quadrature scheme, we can solve (13) by discretizing and turning that equation into a straightforward matrix inversion. Some care is needed because the Green function has logarithmic singularities, and we follow the guidelines set down by Petrelis et al. (2006). The singularities can be removed by first dividing up the interval $0 \le X, X' \le \pi$ into a grid $\{X_m, X'_n\}$ (for $0 \le m$ and $n \le N$ for some N), and then integrating (13) over each of the resulting segments. Provided the grid is sufficiently fine, we arrive at the approximate system

$$\frac{1}{2}\Delta(H_m + H_{m-1}) = \sum_{n=1}^{N} \Gamma_{n-\frac{1}{2}} \int_{X_{m-1}}^{X_m} \int_{X_{n-1}}^{X_n} \mathcal{G}[X, X', \epsilon H(X), \epsilon H(X')]dX\,dX', \quad (14)$$

where $\Gamma_{n-1/2} = [\Gamma(X_n) + \Gamma(X_{n-1})]/2$. The integrals can be evaluated straightforwardly to complete the matrix inversion problem using the approximations

$$H(X) \approx H_{m-1/2} + H'_{m-1/2}(X - X_{m-1/2}) \quad \text{and}$$
$$H(X') \approx H_{n-1/2} + H'_{n-1/2}(X' - X_{n-1/2}),$$

where the subscripts $n - \frac{1}{2}$ and $m - \frac{1}{2}$ indicate averages over the nth and mth segments, or, just as accurately, the values at the midpoints. Typically, we used about 10^3 spatial grid points [max(n)] and 10^4 terms in the Fourier series [max(p)].

c. The conversion rate

Along horizontal sections above the crests of the topography, the solution simplifies to the series,

$$\varphi = \sum_{p=1}^{\infty} \frac{1}{p} \hat{\Gamma}_p \cos pX e^{-ipZ} + \frac{i\epsilon}{\pi} \int_0^{\pi} H(X')\Gamma(X')dX', \quad (15)$$

where

$$\hat{\Gamma}_p(\epsilon, \gamma) = \frac{1}{\pi} \int_0^{\pi} \Gamma(X) \cos pX [e^{ip\epsilon H(X)} - e^{-ip\epsilon H(X)}]dX. \quad (16)$$

This alternative form of the solution is useful in calculating the conversion rate.

Following Balmforth et al. (2002), the (dimensional) conversion rate can be determined to be given by

$$\mathcal{C} = \frac{\rho U^2 h_m^2}{2i\omega} \sqrt{(N^2 - \omega^2)(\omega^2 - f^2)} \int_0^{\pi} (\varphi \varphi_Z^* - \varphi^* \varphi_Z)dX. \quad (17)$$

Using the decomposition (15), we rewrite this in the form of

$$\mathcal{C} = \frac{\pi \rho b^2 U^2}{8\omega} \sqrt{(N^2 - \omega^2)(\omega^2 - f^2)}\, M(\epsilon, \gamma), \quad (18)$$

where

$$M(\epsilon, \gamma) = \frac{4h_m^2}{b^2} \sum_{p=1}^{\infty} \frac{1}{p} |\hat{\Gamma}_p|^2 \quad (19)$$

contains the detailed dependence on the topographic shape through both the Fourier coefficients $\hat{\Gamma}_p(\epsilon, \gamma)$, and the prefactor $4h_m^2/b$.

Along the lines pointed out by Petrelis et al. (2006), an alternative formula for $M(\epsilon, \gamma)$ follows from inserting the definition of Γ_p into (19) and using the integral (13), giving

$$M(\epsilon, \gamma) = \frac{h_m^2}{b^2} \int_0^{\pi} H(X)\Gamma_r(X) \frac{dX}{\pi}, \quad (20)$$

where $\Gamma_r \equiv \mathrm{Re}(\Gamma)$. A comparison of numerical values of (19) and (20) offers a useful check of computational accuracy.

3. Results

a. The sinusoid ($\gamma = 0$)

Figure 1 shows a sample calculation for supercritical sinusoidal topography. The source density develops

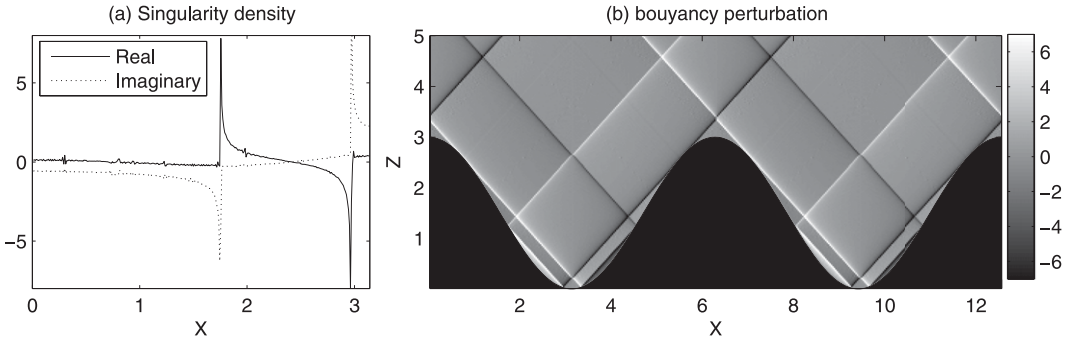

FIG. 1. Scattering from supercritical sinusoidal topography with $\epsilon = 1.5$. (a) Shown is $\Gamma(X)$ and (b) a snapshot of the dimensionless buoyancy perturbation $\mathrm{Re}(-i\varphi_X)$ at $t = 0$. Note the residual noise in $\Gamma(X)$, generated by the inadequacy of the numerical scheme to cope properly with the sharp features in $\Gamma(X)$ occurring where the beams intersect the topography. The shading levels used to plot the buoyancy perturbation in (b) are chosen so that saturation occurs well below the extremal values reached by the solution. This device is used in all subsequent plots of radiated buoyancy fields and is essential to removing the dependence of the plot on the truncation of the sums in (12) and (14), which renders the solution finite.

sharp, singular peaks that can be traced to upward and downward propagating wave beams that leave the topography at the points with critical slope, and, in particular, where these beams subsequently reflect off the bottom. The beams, which dominate the radiated buoyancy field, are formally divergent in inviscid wave theory, as noted by previous authors (Balmforth et al. 2002; Petrelis et al. 2006). In the numerical calculations, the buoyancy perturbations are actually made finite by the truncation of the spatial and Fourier sums in (12) and (14). A more controlled smoothing procedure is to add explicitly a viscous correction (cf. Peacock et al. 2008). In the graphical representation of the radiated buoyancy field, the shading levels saturate well below the extremal values reached, rendering the plot independent of the precise truncation used (or, equivalently, the size of any viscous correction).

Note that wave beams can only be emitted from the uppermost points of critical slope, where the topography is convex. Also, with a smooth bottom profile, the downward propagating wave beams must always eventually encounter a subcritical slope and therefore become reflected back upward, thereby escaping any topographic traps.

Sample conversion rates $M(\epsilon, 0)$ for the sinusoidal topography are shown in Fig. 2. The results for subcritical topography match the earlier calculations of Balmforth et al. (2002) and increase from unity at $\epsilon = 0$ (Bell's limit) up to about 1.56 at criticality. The conversion rate increases a little farther beyond $\epsilon = 1$, up to a maximum value just above 2 but then abruptly declines and begins a series of decaying oscillations with ϵ. As illustrated by the top row of wavefields in the figure, the conversion rate peaks when all the upward propagating wave beams follow similar paths and have a common overall phase at levels above the crests of the topography. The minima of $M(\epsilon, 0)$, on the other hand, correspond to instances wherein the beams follow similar paths but have an opposite overall phase (the lower row of wavefields). Thus, we conclude that the peaks and troughs are caused by constructive and destructive interferences among the beams within the scattered wavefield, as found for other topography by Petrelis et al. (2006) and Nycander (2006). Note that, although the beams are merely following characteristic lines at 45°, it is the concentration of the wavefield in these structures that is key to the patterns of interference, which become increasingly complex with increasing ϵ, as shown in Fig. 2.

b. The periodic Gaussian

A sample solution for a periodic Gaussian (with $\gamma = 10$ and $\epsilon = 2$) is shown in Fig. 3. Note that the Green function solution can also provide a solution for ''inverted'' topography, corresponding to scattering by a periodic array of trenches. The second panel of Fig. 3 illustrates both wavefields.

Conversion rates for periodic Gaussians are shown in Fig. 4. For $\epsilon \to 0$, the conversion rate converges to a γ -dependent value between 1 (the rate for a sinusoid, given by $\gamma = 0$) and $4/\pi$ (the conversion for an isolated Gaussian bump with $\gamma \to \infty$). Sufficiently far above criticality, the conversion rate again passes through a sequence of constructive and destructive interferences. For the more widely separated obstacles ($\gamma = 4$ and higher), the conversion rate initially flattens out close to 2 before the beginning of the interference sequence, which is the value expected for an isolated knife edge (Llewellyn Smith and Young 2003; Nycander 2006).

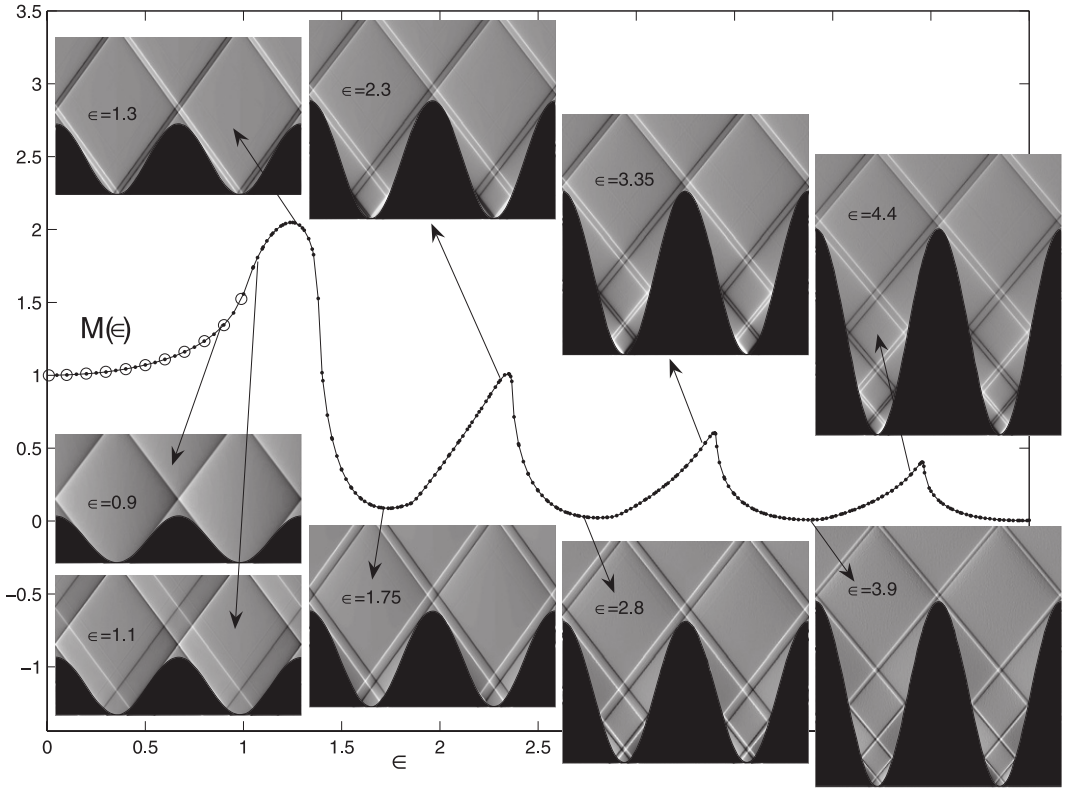

FIG. 2. The dimensionless conversion rate and a series of snapshots (at $t = 0$) of the buoyancy perturbation of the wavefield for the sinusoidal topography. Arrows indicate the ε values of the snapshots, and the circles show the subcritical results of Balmforth et al. (2002).

Conversion rates for Gaussian ridges and trenches are compared in Fig. 5. When the topography is subcritical, the conversions are identical, as noted by Balmforth et al. (2002). However, once the slopes become supercritical, this no longer remains the case. As is clear from Fig. 3, the trench suffers a more complicated pattern of interferences than the ridge, leading to faster oscillations in the conversion rate. The conversion is on the whole much less for the trench than the ridge. It is also almost independent of γ once the obstacles are sufficiently far apart (γ sufficiently large), reflecting how the scattering is localized and directed away from neighboring trenches, with interference occurring only within each trench.

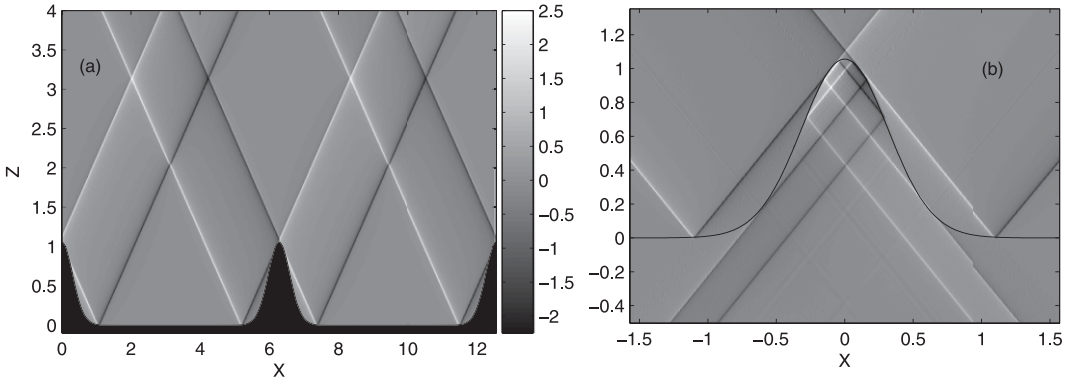

FIG. 3. Scattering from periodic Gaussian topography with $\epsilon = 2$ and $\gamma = 10$. (a) Shown is the buoyancy perturbation of the up-going wave field $\mathrm{Re}(-i\varphi_X)$. (b) Shown is a magnification around the Gaussian bump and both the up-going wavefield from a Gaussian bump and the down-going wavefield from a Gaussian trench.

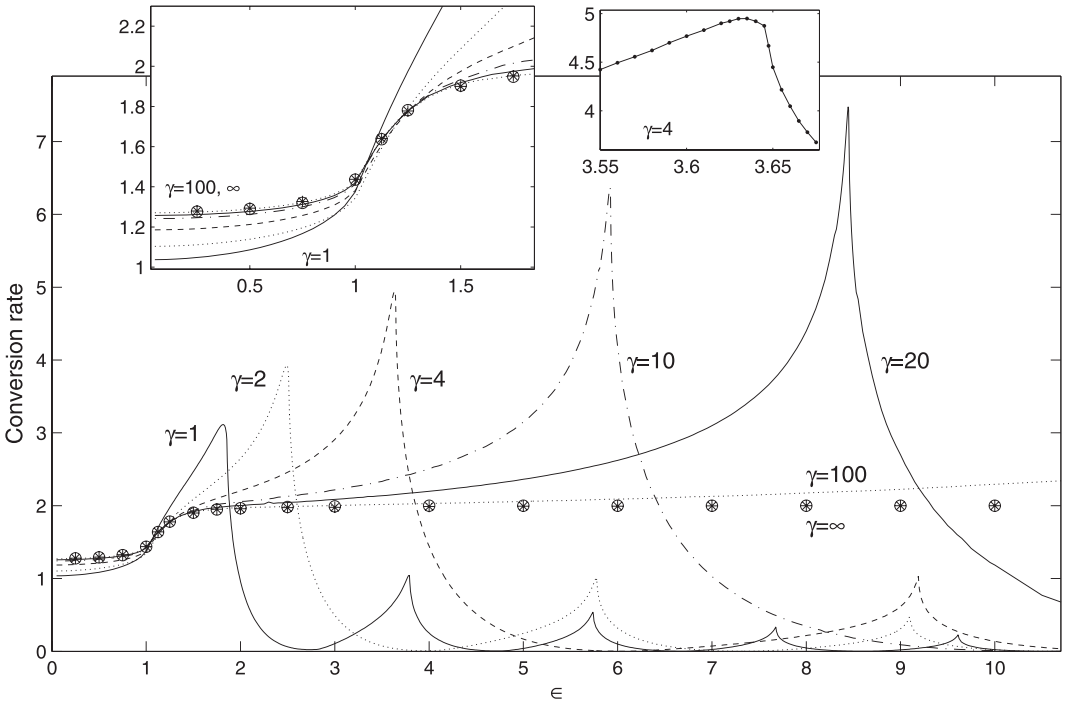

FIG. 4. Conversion rates, $M(\epsilon, \gamma)$, for periodic Gaussian topography with $\gamma = 1, 2, 4, 10, 20$, and 100. The points show a computation for an isolated Gaussian ($\gamma \to \infty$) obtained using the methods of Petrelis et al. (2006). The two insets focus in on conversion rates for near-critical topography and for a peak in the conversion rate.

Despite the oscillatory structure in the conversion rates introduced by the interference sequence displayed in Figs. 2, 4, and 5, the overall trend is for $M(\epsilon, \gamma)$ to decrease for large ϵ (the curves for $\gamma = 20$ and 100 in Fig. 4 follow the trend only for higher values of ϵ than those shown, as do the ridge conversion rates shown in Fig. 5). This fall off with topographic amplitude (as incorporated in ϵ) is deceiving in view of the dimensional prefactor of the complete conversion rate $\mathcal{C}$ in (18), which contains b^2. To emphasize the main dependence on topographic amplitude, we must extract the b^2 from the prefactor in a suitable dimensionless form and then include that combination in $M(\epsilon, \gamma)$. Following Nycander (2006), we write the dimensional conversion rate in the alternative form

$$\mathcal{C} = \frac{\rho U^2}{\omega k^2}(\omega^2 - f^2)\sqrt{\frac{(\omega^2 - f^2)}{(N^2 - \omega^2)}}I(B, \gamma), \tag{21}$$

where

$$I(B, \gamma) = \frac{\pi}{8}B^2 M(\epsilon, \gamma), \quad \text{and} \tag{22}$$

$$B \equiv kb\sqrt{\frac{N^2 - \omega^2}{\omega^2 - f^2}} = \frac{\epsilon b}{h_m} \tag{23}$$

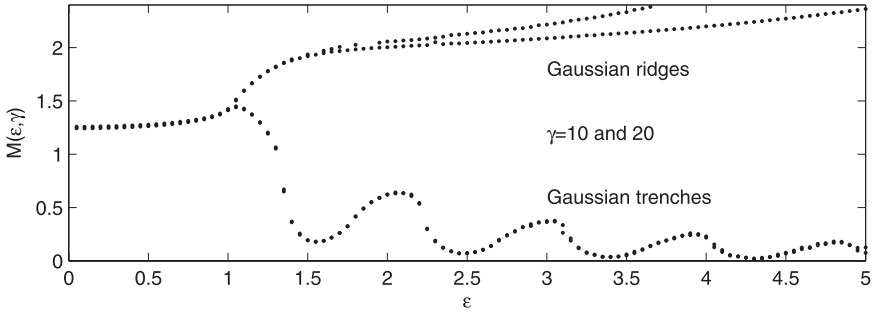

FIG. 5. The dimensionless conversion rates for periodic Gaussian ridges and trenches with $\gamma = 10$ and 20. The two sets of results for different γ are distinguishable only for the case of Gaussian ridges, where the conversion for $\gamma = 10$ is higher than that for $\gamma = 20$.

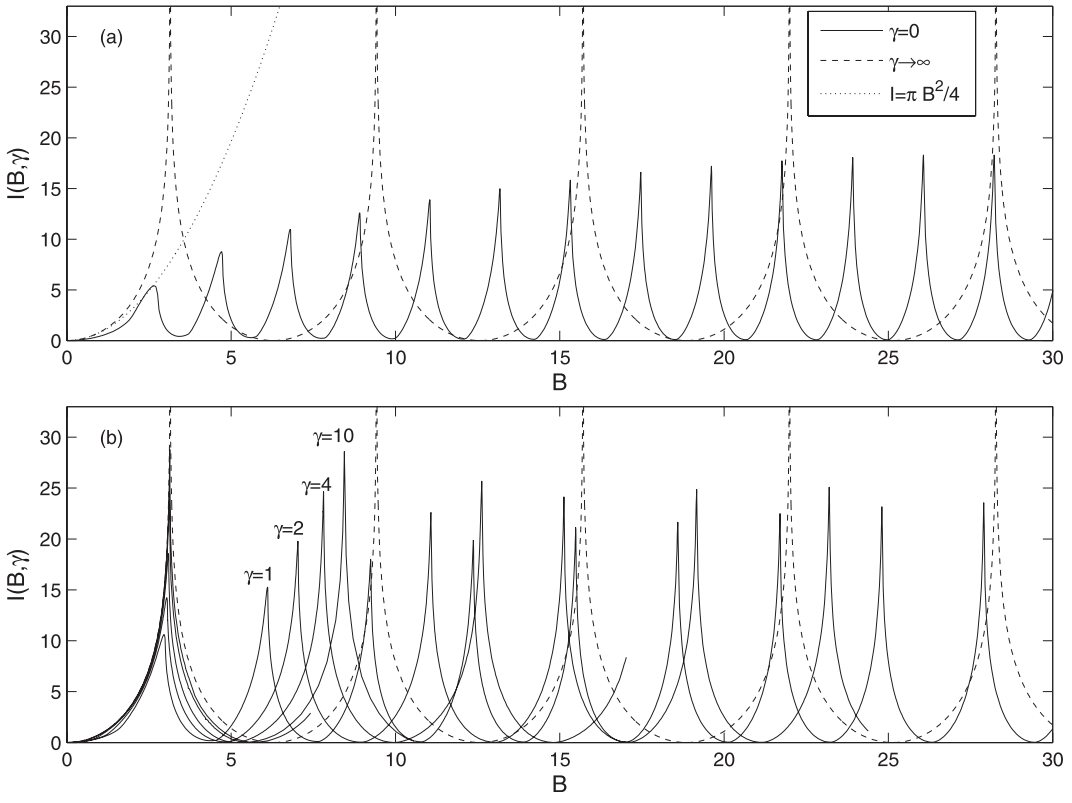

FIG. 6. Rescaled conversion rate I against the dimensionless height parameter B for (a) sinusoidal ($\gamma = 0$) and (b) periodic Gaussian topography ($\gamma = 1$, 2, 4, 10, and 20). Also indicated are results for Nycander's periodic array of knife edges (dashed curve) and an isolated knife edge [dotted curve in (a)]. Note that the results for the periodic Gaussian were computed for the range $0 \le \epsilon \le 20$, which corresponds to varying ranges of B for different γ values (e.g., the $\gamma = 20$ curve ends just above $B = 7$).

is a new dimensionless parameter giving the topographic amplitude in terms of an alternative vertical length scale based on the separation of the obstacles scaled by the wave slope (and which is used in the new prefactor of $\mathcal{C}$).

The function $I(B, \gamma)$ expresses a new dimensionless conversion rate in terms of B and the shape parameter γ and is shown in Fig. 6 for the periodic Gaussian ridges. The oscillations of $I(B, \gamma)$ no longer decrease in strength with B. Also included in the figure is the curve

$$I(B, \gamma \to \infty) \equiv \int_0^B \sqrt{\frac{1 - \cos z}{\cos z - \cos B}}\, z\, dz, \qquad (24)$$

which is Nycander's result for a periodic array of knife edges and the result expected for an isolated knife edge, $I = \pi B^2/4$ (Llewellyn Smith and Young 2003). Note that, for a periodic array of knife edges, the positions of the "resonant" peaks in the conversion rate occur when $B = (2m + 1)\pi$, whereas the minima of $I(B, \gamma \to \infty)$ arise for $B = 2m\pi$. For the periodic Gaussians, the resonance peaks are shifted with respect to Nycander's knife edges as a result of the finite width and slopes.[3] Moreover, the peaks in conversion are finite, in contrast to the singular peaks for the knife edge resonances, which diverge logarithmically.

4. Summary

Once the maximum topographic slope exceeds that of the scattered gravity waves, singular beams radiate away from points on the topography with critical slope, which are locally convex (which guarantees that the scattered waves lie within the fluid). The up- and down-going beams can interfere with one another, either constructively or destructively, once the latter have been reflected back up. The pattern of constructive and destructive interference that results when one changes the height of the topography is reflected in an oscillatory rate of energy conversion. Our main results have been for periodic

[3] As pointed out to us by Jonas Nycander, a straighforward geometrical construction furnishes the modified peak positions.

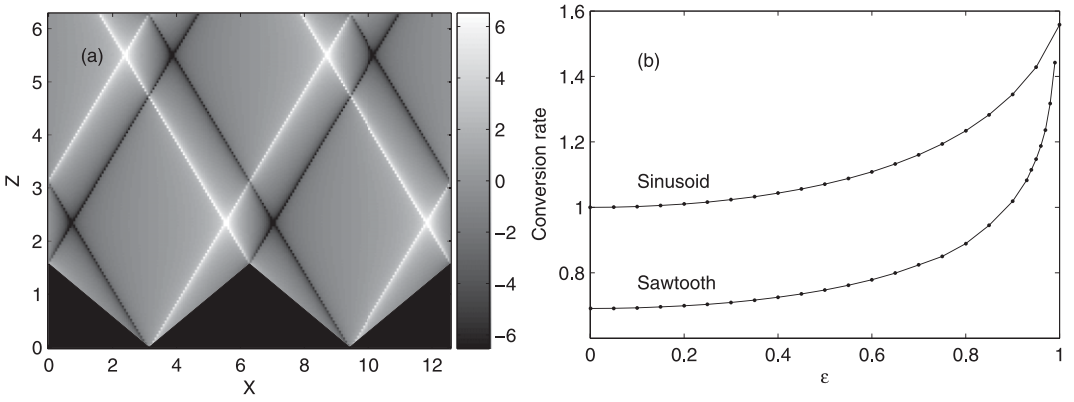

FIG. 7. (a) Shown is the buoyancy perturbation induced by waves scattered from a sawtooth-shaped topography for $\epsilon = 0.5$. (b) Illustrated is the conversion rate for $\epsilon < 1$.

arrays of Gaussian ridges, although we have also presented energy conversion rates for Gaussian-shaped trenches, finding the latter to be much less efficient at generating internal tides in supercritical regimes.

Although we have explored periodic topography, the results indicate that the supercritical conversion rate of extended topography depends sensitively on the details of the geometry because this in turn controls the pattern of interference. Consequently, in ocean settings where the topography is nominally two-dimensional yet irregular [as in the ''random topography'' considered by Balmforth et al. (2002)], it would be difficult to predict a typical conversion rate. The best we can do given the current results is to report that conversion rate $I(B, \gamma)$, when averaged over an oscillation of the interference sequence, gives a value of around 4 for each γ (cf. Fig. 6). Thus, a crude estimate in a general supercritical situation is

$$\mathcal{C} \sim \frac{4\rho U^2}{\omega k^2}(\omega^2 - f^2)\sqrt{\frac{(\omega^2 - f^2)}{(N^2 - \omega^2)}}, \qquad (25)$$

which may prove a useful parameterization in predicting tidal conversion rates of the global ocean. Note that, as anticipated by Nycander (2006), this average conversion rate is independent of topographic height, unlike the results for isolated topography (e.g., Petrelis et al. 2006).

Nevertheless, the preceding discussion fails to take into account the fact that real topography is three-dimensional. In such situations we envisage that the proximity of neighboring peaks will have less of an effect on the conversion rate because geometrical spreading weakens the wave beams as they propagate, unlike in two dimensions. It is not even clear whether the conversion rate saturates with increasing height of three-dimensional topography.

We close with a comment on a curious feature of another topographic shape—the sawtooth profile. This profile has the property that waves are always scattered from each of its faces in the same direction. For subcritical sawtooths, the wavefield propagates upward and generates wavefields like that illustrated in Fig. 7; the sharp divisions emanating from the corners of the sawtooth develop into beams in the buoyancy field. Also shown in the figure is the conversion rate for $\epsilon < 1$. When the topography is supercritical, on the other hand, waves always scatter downward. In contrast to most other profiles, there is no deeper portion of the topography with gentler slope that can reflect these waves back upward. Thus, the lower points of the sawtooth become wave attractors. In this circumstance it does not seem possible to obtain a stationary, regular scattering state. Indeed, our computations do not converge for $\epsilon \geq 1$, and the conversion rate looks to diverge as $\epsilon \to 1$. It is not clear how physical this situation could be. Nevertheless, it suggests that there may be some interesting wave dynamics, and possibly mixing, at the bottom of steep-sided troughs.

Acknowledgments. This work was supported by the Office of Naval Research Grant N00014-0501-0575 and the National Science Foundation Award 0645529. We thank Bill Young, Stefan Llewellyn Smith, and Jonas Nycander for discussions.

APPENDIX

The Green Function

We derive two equivalent forms for our Green function that prove useful in the calculations of the main text. We borrow heavily from previous work by Petrelis

et al. (2006) and Nycander (2006), although the final form of the Green function that we use is different, owing to the different geometry of the problem.

The Green function for a single source on an infinite plane follows from solving the equation

$$G_{XX} - G_{ZZ} = i\delta(X)\delta(Z), \tag{A1}$$

subject to the radiation condition applying for $|Z| \to \infty$ at fixed X. By Fourier transforming, or other means, we arrive at

$$\begin{aligned} G(X,Z) &= -\frac{1}{4\pi}\int_{-\infty}^{\infty} e^{ikX-i|kZ|}\frac{dk}{|k|} \\ &\equiv -\frac{1}{4\pi}\log|X^2 - Z^2| - \frac{i}{4}\Theta(|Z| - |X|), \end{aligned} \tag{A2}$$

where $\Theta(x)$ is the Heaviside step function.

We build the solution to our full problem by first summing Green function solutions for the original source at $(X, Z) = (X', Z')$ and all its periodic images:

$$G_P(X - X', Z - Z') = \sum_{n=-\infty}^{\infty} G(X - 2n\pi - X', Z - Z'). \tag{A3}$$

We then account for the $X \to 2\pi - X$ symmetry of the profile and solution by adding more sources at the periodic reflections, $(X, Z) = (2n\pi - X', Z')$. Last, we add negative sources at $(X, Z) = (2n\pi + X', -Z')$ and $(X, Z) = (2n\pi - X', -Z')$ to ensure that the solution vanishes wherever the topography decays and $H(X) = 0$. Thus, our complete Green function is

$$\begin{aligned} \mathcal{G}(X,X',Z,Z') = {} & G_P(X - X', Z - Z') \\ & + G_P(X + X', Z - Z') \\ & - G_p(X - X', Z + Z') \\ & - G_p(X + X', Z + Z'). \end{aligned} \tag{A4}$$

The real part of this Green function contains four sets of terms, such as

$$\frac{1}{4\pi}\sum_{n=1}^{\infty}\log\left|\frac{4n^2\pi^2 - (X - X' - Z + Z')^2}{4n^2\pi^2 - (X - X' - Z - Z')^2}\right|. \tag{A5}$$

By using the relation

$$\sum_{n=1}^{\infty}\log\left|1 - \frac{x^2}{n^2}\right| = \log|\sin x| - \log|x|, \tag{A6}$$

we may sum each of these terms explicitly, and we arrive eventually at

$$\mathcal{G}(X,X',Z,Z') = \mathcal{G}_r(X,X',Z,Z') + i\mathcal{G}_i(X,X',Z,Z'), \tag{A7}$$

where

$$\mathcal{G}_r(X,X',Z,Z') = -\frac{1}{4\pi}\log|\bowtie(X,X',Z,Z')| - \frac{1}{\pi}\log 2, \tag{A8}$$

and

$$\begin{aligned} \mathcal{G}_i(X,X',Z,Z') \equiv {} & \frac{1}{4}\sum_{-\infty}^{\infty}[\Theta(|Z + Z'| - |X - X' + 2n\pi|) + \Theta(|Z + Z'| - |X + X' + 2n\pi|)] \\ & - \frac{1}{4}\sum_{-\infty}^{\infty}[\Theta(|Z - Z'| - |X - X' + 2n\pi|) + \Theta(|Z - Z'| - |X + X' + 2n\pi|)] \end{aligned} \tag{A9}$$

(which is a finite sum for any given distance from the original source), with

$$\bowtie = \frac{\sin\frac{1}{2}(X - X' - Z + Z')\sin\frac{1}{2}(X - X' + Z - Z')\sin\frac{1}{2}(X + X' - Z + Z')\sin\frac{1}{2}(X + X' + Z - Z')}{\sin\frac{1}{2}(X - X' - Z - Z')\sin\frac{1}{2}(X - X' + Z + Z')\sin\frac{1}{2}(X + X' - Z - Z')\sin\frac{1}{2}(X + X' + Z + Z')}. \tag{A10}$$

Alternatively, $\mathcal{G} = (4\pi)^{-1}\log(16\bowtie)$, with the understanding that (A9) offers a means to sort out explicitly how to extract the imaginary part.

An equivalent expression comes from solving the alternative problem

$$\mathcal{G}_{XX} - \mathcal{G}_{ZZ} = i[\delta(Z - Z') - \delta(Z + Z')]\sum_{n=-\infty}^{\infty}[\delta(X - X' - 2n\pi) + \delta(X + X' - 2n\pi)], \tag{A11}$$

subject to the radiation condition and using a Fourier cosine series in X [including the zero wavenumber component, which leads to the final term in (12)]. The result (12) can also be derived directly from (A10) by turning the sines into exponentials and then using the Taylor series expansion of the logarithm together with some common trigonometric relations.

REFERENCES

Balmforth, N. J., G. R. Ierley, and W. R. Young, 2002: Tidal conversion by subcritical topography. *J. Phys. Oceanogr.,* **32,** 2900–2914.

Bell, T. H., 1975a: Lee waves in stratified fluid with simple harmonic time dependence. *J. Fluid Mech.,* **67,** 705–722.

——, 1975b: Topographically generated internal waves in the open ocean. *J. Geophys. Res.,* **80,** 320–327.

DiLorenzo, E., W. R. Young, and S. G. Llewellyn Smith, 2006: Numerical and analytical estimates of M_2 tidal conversion at steep oceanic ridges. *J. Phys. Oceanogr.,* **36,** 1072–1084.

Egbert, G. D., and R. D. Ray, 2000: Significant dissipation of tidal energy in the deep ocean inferred from satellite altimeter data. *Nature,* **405,** 775–778.

Garrett, C., and E. Kunze, 2007: Internal tide generation in the deep ocean. *Annu. Rev. Fluid Mech.,* **39,** 57–87.

Khatiwala, S., 2003: Generation of internal tides in an ocean of finite depth: Analytical and numerical calculations. *Deep-Sea Res. I,* **50,** 3–21.

Llewellyn Smith, S., and W. R. Young, 2003: Tidal conversion at a very steep ridge. *J. Fluid Mech.,* **495,** 175–191.

Munk, W. H., and C. I. Wunsch, 1998: Abyssal recipes II: Energetics of tidal and wind mixing. *Deep-Sea Res. I,* **45,** 1977–2010.

Nycander, J., 2005: Generation of internal waves in the deep ocean by tides. *J. Geophys. Res.,* **110,** C10028, doi:10.1029/2004JC002487.

——, 2006: Tidal generation of internal waves from a periodic array of steep ridges. *J. Fluid Mech.,* **567,** 415–432.

Peacock, T., P. Echeverri, and N. J. Balmforth, 2008: An experimental investigation of internal tide generation by two-dimensional topography. *J. Phys. Oceanogr.,* **38,** 235–242.

Petrelis, F., S. G. Llewelyn Smith, and W. R. Young, 2006: Tidal conversion at a submarine ridge. *J. Phys. Oceanogr.,* **36,** 1053–1071.

St. Laurent, L., S. Stringer, C. J. R. Garrett, and D. Perrault-Joncas, 2003: The generation of internal tides at abrupt topography. *Deep-Sea Res. I,* **50,** 987–1003.